Reaction Kinetics, Mechanisms and Catalysis (2020) 131:613–644
https://doi.org/10.1007/s11144-020-01896-4

Dynamic modeling and simulation of three-phase reactors for hydrocracking of vegetable oils

Fabián S. Mederos-Nieto[1,2] · Ignacio Elizalde-Martínez[1] · Fernando Trejo-Zárraga[3] · Raúl Hernández-Altamirano[1,2] · Fernando Alonso-Martínez[4]

Received: 31 August 2020 / Accepted: 18 October 2020 / Published online: 27 October 2020

Abstract

A dynamic, plug-flow, one-dimensional, and heterogeneous mathematical model for a trickle-bed reactor is described and used to simulate the catalytic hydrocracking of non-edible vegetable oil with countercurrent operation mode. The reactor model considers the hydrocracking reaction of triglycerides towards renewable fuels, which is present in the hydrotreatment process of vegetable oils. The dynamic model was first validated using experimental data reported in the literature, which were obtained in an isothermal micro-scale reactor with cocurrent downflow during hydrocracking of *Jatropha* oil over a commercial CoMo catalyst. Then, the three-phase reactor model was applied to predict the dynamic behavior of an industrial hydrocracking reactor in order to gain some insight into the transient behavior of the liquid molar concentration, partial pressure, and temperature profiles, which were obtained and discussed as a function of time and axial position of the catalytic bed. The simulations obtained with the proposed dynamic model showed good agreement with the experimental data and trends previously reported for the operation variables profiles at steady-state and relevant findings at industrial scale were obtained.

Graphic abstract

One of the main challenges to produce biofuels by vegetable oils hydroprocessing is to control the high-temperature gradients along the catalyst bed because of the

✉ Fabián S. Mederos-Nieto
fabmederos@yahoo.com.mx

[1] Instituto Politécnico Nacional, Centro Mexicano Para la Producción Más Limpia (CMPL), Posgrado, Av. Acueducto s/n, Col. La Laguna Ticomán, C.P. 07340 Mexico City, Mexico

[2] Instituto Politécnico Nacional, Laboratorio Nacional de Desarrollo y Aseguramiento de la Calidad de Biocombustibles (LaNDACBio), Av. Acueducto s/n, Col. La Laguna Ticomán, C.P. 07340 Mexico City, Mexico

[3] Instituto Politécnico Nacional, CICATA-Legaria, Legaria 694, Col. Irrigación, C.P. 11500 Mexico City, Mexico

[4] Instituto Politécnico Nacional, ESIQIE, UPALM, Zacatenco, Edificio 8, C.P. 077380 Mexico City, Mexico

high reaction heat released; therefore, the development of dynamic trickle-bed reactor models, as shown in this work, can be used as a tool to predict the operational behavior of the unit under different reaction conditions and layouts to found the best scheme to control the effects by high-temperature rise.

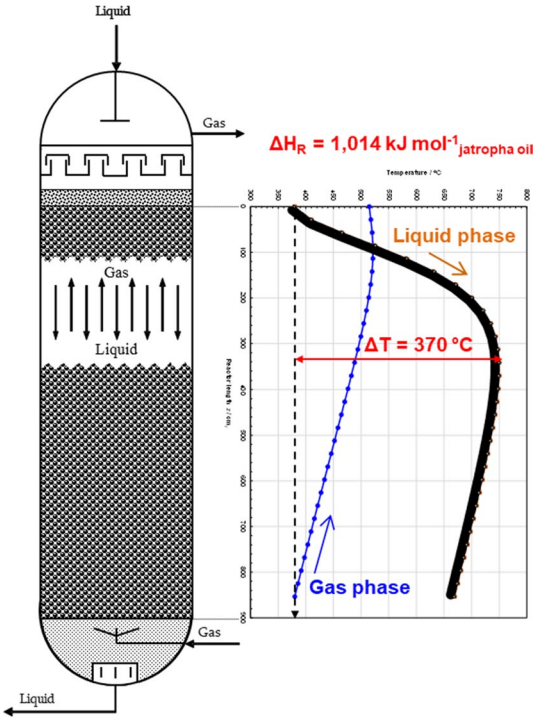

Keywords Renewable fuels · Dynamic modeling · Hydrocracking · Vegetable oils · Trickle-bed reactor · *Jatropha* oil

List of symbols

a_L ($cm^2_I\ cm^{-3}_r$)	Specific gas–liquid interfacial area per unit volume of the bed
a_S ($cm^2_S\ cm^{-3}_r$)	Specific external surface area of catalyst per unit volume of the bed
a_w ($cm^2_{S,wet}\ cm^{-3}_r$)	Freshly wetted external area per unit volume of bed
C_d (–)	Constant for Eq. 25
Cp_f ($J\ g^{-1}_f\ K^{-1}$)	Specific heat capacity of *f* phase
C_i^L ($mol_i\ cm^{-3}_L$)	Molar concentration of component *i* in the bulk liquid phase
C_{SLi}^S ($mol_i\ cm^{-3}_L$)	Molar concentration of component *i* at surface of solid covered by liquid phase
d_{pe} (cm_S)	Equivalent catalyst particle diameter

d_R (cm_r)	Inside reactor diameter
D^f_{ei} ($cm^3{}_f\,cm^{-1}{}_s\,s^{-1}$)	Effective diffusion coefficient of compound *i* in the *f* phase
D^f_{Mi} ($cm^3{}_f\,cm^{-1}{}_s\,s^{-1}$)	Molecular diffusion coefficient of compound *i* in the *f* phase
D^f_{Ki} ($cm^3{}_f\,cm^{-1}{}_s\,s^{-1}$)	Knudsen diffusion coefficient of compound *i* in the *f* phase
$E_{a,j}$ ($J\,mol^{-1}{}_i$)	Activation energy for *j* reaction
f_w ($cm^2{}_{S,wet}\,cm^{-2}{}_S$)	Catalyst wetting efficiency
f^L_i (MPa)	Liquid phase fugacity of compound *i*
F ($g_i\,g^{-1}{}_L$)	Objective function to be optimized
g ($cm_r\,s^{-2}$)	Acceleration due to the gravity (981)
G_f ($g_f\,cm^{-2}{}_r\,s^{-1}$)	Superficial mass-flow velocity of *f* phase
h_f ($J\,cm^{-2}{}_I\,s^{-1}\,K^{-1}$)	Phase *f*-film heat-transfer coefficient
h_{GL} ($J\,cm^{-2}{}_I\,s^{-1}\,K^{-1}$)	Overall heat-transfer coefficient at the gas–liquid interface
h_{LS} ($J\,cm^{-2}{}_S\,s^{-1}\,K^{-1}$)	Heat-transfer coefficient for liquid film at the liquid–solid interface
H_i ($MPa\,cm^3{}_L\,mol^{-1}{}_i$)	Henry's law coefficient of component *i*
k_j (s^{-1})	Rate constant of reaction *j* (= *TG*, 1, 2, 3, 4, 5, and 6)
$k_{0,j}$ (s^{-1})	Frequency or pre-exponential factor
k^f_i ($cm^{-3}{}_f\,cm^{-2}{}_I\,s^{-1}$)	Phase *f*-film mass-transfer coefficient of compound *i*
k^S_i ($cm^3{}_L\,cm^{-2}{}_S\,s^{-1}$)	Liquid–solid mass-transfer coefficient of compound *i*
K_{Li} ($cm^3{}_L\,cm^{-2}{}_I\,s^{-1}$)	Overall volumetric G-L mass-transfer coefficient of compound *i* in liquid phase
L_B (cm_r)	Catalyst bed length
$LHSV$ ($cm^3{}_L\,cm^{-3}{}_{cat}\,h^{-1}$)	Liquid hourly space velocity
MW_f ($g_f\,mol^{-1}{}_f$)	Molecular weight of *f* phase
n (–)	HDC reaction order
n_S (–)	Empirical coefficient for Eq. 28
N_{exp} (–)	Number of experiments
N_{lump} (–)	Number of lumps
p^G_i (MPa)	Partial pressure of component *i* in the bulk gas phase
P_v (MPa)	Vapor pressure of the liquid phase at its corresponding temperature
P (MPa)	Total operating pressure
r^L_j ($mol_i\,cm^{-3}{}_L\,s^{-1}$)	Rate of reaction *j* per unit of volume in the liquid phase
r'^L_j ($mol_i\,g^{-1}{}_S\,s^{-1}$)	Rate of reaction *j* per unit of catalyst mass in the liquid phase
R ($J\,mol^{-1}{}_i\,K^{-1}$)	Universal gas law constant (8.314471)
S_p ($cm^2{}_S$)	Total geometric external surface area of catalyst particle
t (s)	Time
T_f (K)	Temperature of *f* phase
T_M (K)	Maximum temperature before hot spots presence
u_f ($cm^3{}_f\,cm^{-2}{}_r\,s^{-1}$)	Superficial velocity of *f* phase

V_p ($cm^3{}_S$)	Total geometric volume of catalyst particle
w_i ($g_i\ g^{-1}{}_L$)	Weight fraction of lump i in the liquid phase
W (–)	The wetting number
x_i ($mol_i\ mol^{-1}{}_L$)	Mole fraction of component i in the liquid phase
X_{TG} (–)	Conversion of TGs
z (cm_r)	Axial reactor coordinate
Z^f (–)	Compressibility factor of f phase

Greek letters

α_S (–)	Empirical coefficient for Eq. 28
$\Delta H^L_{R,j}$ ($J\ mol^{-1}{}_i$)	Heat of reaction j in the liquid phase
ΔT_{ad} (K)	Adiabatic temperature rise
$\Delta P/\Delta z$ ($N\ m^{-3}$)	Pressure gradient
ε_f ($cm^3{}_f\ cm^{-3}{}_r$)	External holdup of f phase
$\in_B$ ($cm^3{}_{(G+L)}\ cm^{-3}{}_r$)	Bed void fraction
$\in_S$ ($cm^3{}_{(G+L)}\ cm^{-3}{}_S$)	Solid particle porosity
ζ ($cm^3{}_{cat}\ cm^{-3}{}_r$)	Catalyst bed dilution factor
η^L_j (–)	Catalyst effectiveness factor of reaction j in the liquid phase
μ_f (cP)	Dynamic viscosity of f phase
ρ_B ($g_S\ cm^{-3}{}_{cat/r}$)	Catalyst bed density
ρ_f ($g_f\ cm^{-3}{}_f$)	Density of f phase
τ ($cm_L\ cm^{-1}{}_S$); (h)	Tortuosity factor for catalyst particle
$v^L_{i,j}$ (–)	Stoichiometric coefficient of component i in reaction j in the liquid phase
ϕ_S (–)	Shape factor = surface area of a sphere of equal volume/particle surface area
ϕ^L_j (–)	Thiele modulus of reaction j in the liquid phase
ϕ^L_i (–)	Liquid phase fugacity coefficient of component i

Dimensionless groups

$Bo^L_{a,m}$	Axial mass Bodenstein number for liquid phase
Ga_f	Galileo number of f phase
Re_f	Reynolds number of f phase

Subscripts

0	Reactor inlet condition; initial conditions
B	Catalyst bed
calc	Calculated
exp	Experimental
f	Gas, liquid or solid phase; reactor outlet condition
i	Component or lump index
I	Gas–liquid interface
j	Reaction index
k	Experiment index; component index

L	Liquid phase
L_B	Reactor outlet condition
S	Solid phase; condition at external surface of catalyst particle

Superscripts

G	Gas phase; gas side of the gas–liquid interface
L	Liquid phase; liquid side of the gas–liquid interface
S	Solid phase; liquid film of the liquid–solid interface

Introduction

Each year, the demand for liquid fuels rises giving as result an equivalent increase in the environmental pollution because of its excessive use and increasingly stringent environmental regulations on emissions of pollutants into the atmosphere; whereby it is necessary to promote research for alternative energy resources. The renewable fuels are a potential alternative for the future, which could provide a main energy source because of its sustainability and compliance with emissions standards [1].

Nowadays, the edible and non-edible vegetable oils are a major source of the feedstock for the production of green or renewable fuels (gasoline, kerosene, and diesel). These vegetable oils mainly consist of triglycerides (TGs) and free fatty acids (FFAs) along with some traces of diglycerides and monoglycerides [2]. A new alternative for production of green fuels is the hydroprocessing (HPR) of a vegetable oil feedstock [3]. This process occurs in the presence of hydrogen at relatively mild-to-high pressures and temperatures similar to those used for hydrotreatment (HDT) of petroleum fractions. On the other hand, the quality of the fuels obtained by this process depends on the activity of the catalyst and operating conditions used. Therefore, the catalytic HPR of vegetable oils is a promising alternative for the production of environmentally friendly fuels, which could use the existing infrastructure in the oil refineries [4, 5].

The conventional HDT process, involves the removal of heteroatoms such as sulfur, nitrogen, and oxygen [6], while the catalytic HPR of vegetable oils involves the transformation of TGs from vegetable oils into linear chain hydrocarbons via hydrodeoxygenation (HDO) reactions followed by reaction paths of conventional hydrocracking (HDC) to generate multiple hydrocarbon compounds similar to that present in light, middle, and heavy petroleum fractions. The HDC process involves cleavage and saturation of C–C bonds in order to produce fuels of high quality such as gasoline, kerosene, and diesel. On the other hand, diesel obtained by catalytic HPR of vegetable oils seems to have better properties in comparison with that obtained by transesterification process [7].

The HDT of blends of vegetable oils and fossil gas oils has been explored for the production of renewable fuels using HDT commercial catalysts such as CoMo/γ-Al_2O_3 and NiMo/γ-Al_2O_3 under normal hydrodesulfurization (HDS) operating conditions. The aim of the HDT process of vegetable oils is to diminish the size of the TGs molecules and to remove oxygen from the vegetable oil by thermal cracking

and isomerization with the addition of H_2 at temperatures between 330 and 360 °C and at pressures between 2 and 9 MPag (20–90 barg). Through this process, it is achieved to transform the vegetable oil into a sulfur-free fuel with excellent properties as diesel fuel [8].

The modeling of trickle-bed reactors (TBRs) for HDT of vegetable oils has only recently received attention; however, most the reports describe pseudo-homogeneous and heterogeneous models on steady-state at bench scale [9–14], while studies on dynamic modeling and simulation with either pseudo-homogeneous or heterogeneous models at large scale are scarce to the best of our knowledge [8, 15]. Hence the main objective of this contribution is to develop in countercurrent operation mode a dynamic, isothermal, plug-flow, one-dimensional, and heterogeneous mathematical model for a micro-scale TBR taking into account the HDC reaction of TGs present in the HDT process of vegetable oils and thus to predict the dynamic behavior of an adiabatic industrial-scale reactor.

Experimental data

Experimental data reported previously by Anand et al. [12] were used in this study. Briefly, *Jatropha curcas* L., whose properties are shown in Table 1, was used as feedstock. CoMo/γ-Al_2O_3 catalyst properties are given in Table 2. According to the original experimental setup [16], the experiments for HPR of pure *Jatropha* oil were carried out in a bench-top micro-reactor with single-zone tubular furnace, in continuous cocurrent down-flow and isothermal mode.

The catalyst mixed with SiC to reduce axial dispersion and stabilize temperature profiles through the catalyst bed was loaded into a stainless steel tubular reactor [21]. The processing conditions for all the catalytic HDT experiments ranged as follows: temperature 320–360 °C, pressure 2–9 MPag, LHSV 0.8–8.0 h^{-1} and H_2 to feed ratio of 500–2000 NL L^{-1}, as it is shown in the first column of Table 3 [12]. The reaction gases were analyzed by gas chromatography. Simulated distillation (ASTM D-2887) of hydrocracking products was also reported.

Reactor model

The model developed to simulate a TBR in countercurrent gas–liquid flow for HDT of vegetable oils at micro, bench, pilot, and industrial scale is dynamic one-dimensional heterogeneous is based on the three-phase dynamic model reported in literature [22].

Assumptions

In the present study the following assumptions were taken into account:

Table 1 Properties of the vegetable oil feedstock [12, 13, 16, 17]

Jatropha curcas L. oil	Value
Molecular weight (g mol^{-1})[a]	890
Density at 15 °C, 1 atm (g cm^{-3})	0.9163
Density at 360 °C, 8 MPag (g cm^{-3})	0.5940
API gravity	22.76
K_{Watson}	11.66
Dynamic viscosity at 25 °C (cP)	21.10
Kinematic viscosity at 40 °C (cSt)	12.46
Sulfur content (ppm_w)	4.50
Olefins content (mol%)	76.00
Chemical composition (wt%)[b]	
Triglycerides	95.0
Diglycerides	2.5
Monoglycerides	0.8
Free fatty acids	1.7
Total	100.0
Fatty acid composition (wt%)	
C16:0 (palmitic)	19.4
C18:0 (stearic)	7.9
C18:1 (oleic)	45.4
C18:2 (linoleic)	27.3
Total	100.0
Ultimate analysis (wt%)	
C	77.01
H	13.60
O[c]	9.39
N[d]	N.D
S[d]	N.D
Total	100.00
Gum content (mg g^{-1})	8.2
TAN or acid value [$mg_{(KOH)}\ g^{-1}{}_{(oil)}$]	3.8
Metal contents (ppm_w)	
Ni	1.00
Cr	0.12
Mo	0.17
Fe	11.30
Mn	0.94
Distillation curve (wt%)[e]	
IBP—250 °C	Nil
250–380 °C	0.2
380 °C—FBP	99.8

[a]Values reported in the open literature [2, 17–19]

[b]Estimated by the FFAs content [20]

[c]By difference

[d]N.D. = no data, i.e., it is less than 0.1 wt% (although a level S of 4.5 ppm_w is detected by S analyzer)

[e]Simdis data from [16], where the cuts IBP (≈150 °C)–250 °C, 250–380 °C, and 380 °C–FBP (≈ 520 °C) are kerosene, diesel, and high boiling range compounds, respectively

Table 2 Properties of the catalyst [12, 13, 16]

Catalyst	Co–Mo
Surface area ($m^2\ g^{-1}$)	262.0
Total pore volume ($cm^3\ g^{-1}$)	0.6
BJH mean pore radius (Å)	30.0
Surface acidity NH_3 (mmol g^{-1})	0.1
O_2 capacity (μmol g^{-1}_{cat})	12.6
Support	Mesoporous γ-Al_2O_3
Particle shape	Trilobe extrudate
BET surface area ($m^2\ g^{-1}$)	298.0
BJH mean pore diameter (nm)	6.1
Pore volume ($cm^3\ g^{-1}$)	1.1
Chemical composition	(wt%)
CoO	4.0
MoO_3	16.0
P_2O_5	1.0
γ-Al_2O_3	79.0
Total	100.0

1. Gas behaves as plug flow.
2. The micro-scale reactor is isothermally and isobarically operated.
3. The industrial adiabatic reactor is isothermal only in the radial direction.
4. Negligible vapor condensation along the catalytic bed.
5. In the micro-scale reactor the gas-side film of gas–liquid mass transfer offers negligible mass resistance.
6. Liquid–solid film mass transfer constitutes the main resistance in micro-scale reactor, while intraparticle mass transfer is limiting step in an industrial reactor.
7. Effectiveness factor in micro-scale reactor is close to the unity.
8. Chemical reactions occur only on catalytic solid surface.
9. Gas and liquid superficial velocities and holdups in the micro- and industrial-scale reactor remain constant through the reactor cross-section and along the whole catalyst bed.
10. The catalyst particles are completely wetted in both micro- and industrial-scale reactor.
11. The catalyst pores are completely filled with liquid phase because of capillary forces.
12. Because there is no information about the catalyst deactivation, it was considered to be lumped together with the reaction rate constant.
13. Temperature inside catalyst particles is the same of liquid phase.

Table 3 Operating conditions and catalyst loading in different reactors

	Experiments [12]	For validation [14]	Scale-up This work
Reactor application			
Scale	Micro	Micro	Industrial
Mode	Cocurrent	Countercurrent	Countercurrent
Type	Isothermal	Isothermal	Adiabatic
Operating variables			
Pressure (MPag)	2–9	8	8
Temperature (ºC)	320–360	380	380
LHSV (h^{-1})	0.8–8.0	8.0	2.66
H_2/Oil volume ratio (NL L^{-1})	500–2000	1500	1500
Gas phase			
Volumetric flow (NL h^{-1})	–	44.5981	248,417,664
Mass flow (g_G s^{-1})	–	0.0011	15,836.39
Superficial velocity ($cm^3{}_G$ $cm^{-2}{}_r$ s^{-1})	–	0.2845	28.87
Composition (mol%)			
H_2	100.00	100.00	81.63
H_2S	–	–	3.06
H_2O	–	–	–
Light hydrocarbons (C_1–C_4)	–	–	15.31
Total	100.00	100.00	100.00
Liquid phase			
Volumetric flow (bbl day^{-1})	–	0.0045	25,000
Mass flow (g_L s^{-1})	–	0.0048	26,684.34
Superficial velocity ($cm^3{}_L$ $cm^{-2}{}_r$ s^{-1})	–	0.0062	0.63
Solid phase			
Particle shape	Powdered	Powder	trilobe extrudate
Catalyst mass (g_S)	2.0000	2.0000	39,404,753.89
Catalyst volume ($cm^3{}_{catlr}$)	2.4000	2.4000	62,272,143.68
Inert volume ($cm^3{}_{inert}$)	2.4000	2.4000	0.00
Bed volume ($cm^3{}_r$)	3.7165	3.7165	62,272,143.68
Bed length (cm_r)	2.8000	2.8000	853.44
Bed porosity [$cm^3{}_{(L+G)}$ $cm^{-3}{}_r$]	–	0.3755	0.5257
Bed bulk density (g_S $cm^{-3}{}_{catlr}$)	–	0.8333	0.6328
Catalyst particle density (g_S $cm^{-3}{}_S$)	–	1.3343	1.3343
Equivalent particle diameter (cm_S)	0.0520	0.0520	0.2540
Catalyst particle diameter (cm_S)	–	–	0.1900
Catalyst particle length (cm_S)	–	–	0.4300
Mean inert particle diameter (cm_{SiC})	0.0362	0.0362	–
Reactor dimensions			
Inside diameter (cm_r)	1.3	1.3	304.8
Total length (cm_r)	30.0	30.0	910.0

The kinetics of HDT reactions is usually studied taking into account the concentration of the main reactants (TGs, H_2, etc.) in the liquid phase. Under this assumption the kinetic model proposed although fit very well the experimental data, is limited to be used only for the range of experimental conditions studied and in many cases only for the experimental setup used [23].

Dynamic mass balances

The mass transfer of the compounds in the countercurrent TBR is described with the following set of partial differential equations (PDEs), taking into account the previous assumptions.

Gas phase

The transient mass-balance equation in the catalyst bed for the compounds present in the gas phase is the following:

$$\frac{\varepsilon_G}{RT_G}\frac{\partial p_i^G}{\partial t} = +\frac{u_G}{RT_G}\frac{\partial p_i^G}{\partial z} - K_{Li}a_L\left(\frac{p_i^G}{H_i} - C_i^L\right) \tag{1}$$

here $i = H_2$. A complete list of variables of Eq. 1 and subsequent mathematical relations are given in the symbol list section.

Liquid phase

The transient mass-balance equation in the catalyst bed for the gaseous compounds present in the liquid phase is given by:

$$\varepsilon_L\frac{\partial C_i^L}{\partial t} = -u_L\frac{\partial C_i^L}{\partial z} + K_{Li}a_L\left(\frac{p_i^G}{H_i} - C_i^L\right) - f_w k_i^S a_S\left(C_i^L - C_{SLi}^S\right) \tag{2}$$

here $i = H_2$.

The model assumes that TGs and hydrocarbon-like products, are nonvolatile; therefore, the transient mass-balance for the liquid compounds is:

$$\varepsilon_L\frac{\partial C_i^L}{\partial t} = -u_L\frac{\partial C_i^L}{\partial z} - f_w k_i^S a_S\left(C_i^L - C_{SLi}^S\right) \tag{3}$$

here $i = TG$, LP, MP, HP, and OP.

Solid phase

The components transported between liquid and solid phases are consumed or produced by chemical reaction at the wet catalyst surface, according to the following first-order ordinary differential equations (ODEs):

$$\in_S\left(1-\in_B\right)\frac{\partial C^S_{SLi}}{\partial t}=f_w k^S_i a_S\left(C^L_i-C^S_{SLi}\right)+\rho_B\sum_{j=1}^{N_{RL}}\upsilon^L_{i,j}\eta^L_j r'^L_j\left(C^S_{SLi},T^S_S\right) \tag{4}$$

here $i=H_2$, *TG*, *LP*, *MP*, *HP*, and *OP*; $j=$ *LP*, *MP*, *HP*, *OP*, *HP–MP*, and *MP–LP*. Because the units of the reaction rates reported elsewhere [12] are based on volume unit of the liquid phase ($\mathrm{mol}_i\ \mathrm{cm}^{-3}{}_L\ \mathrm{s}^{-1}$), it is necessary to take into account the following equality in order to use the Eqs. 4 and 8:

$$\rho_B r'^L_j=\in_S\left(1-\in_B\right)r^L_j \tag{5}$$

Dynamic energy balances

Since the HDT reactions are exothermic by nature, the energy-balance equations for modeling the industrial HDT reactor operating under non-isothermal conditions in countercurrent operation mode need to be included as given by the following three equations [24]:

(a) Gas phase

$$\varepsilon_G\rho_G Cp_G\frac{\partial T_G}{\partial t}=+u_G\rho_G Cp_G\frac{\partial T_G}{\partial z}-h_{GL}a_L\left(T_G-T_L\right) \tag{6}$$

(b) Liquid phase

$$\varepsilon_L\rho_L Cp_L\frac{\partial T_L}{\partial t}=-u_L\rho_L Cp_L\frac{\partial T_L}{\partial z}+h_{GL}a_L\left(T_G-T_L\right)-f_w h_{LS}a_S\left(T_L-T^S_S\right) \tag{7}$$

(c) Solid phase

$$\varepsilon_S\rho_S Cp_S\frac{\partial T^S_S}{\partial t}=f_w h_{LS}a_S\left(T_L-T^S_S\right)+\upsilon_B\sum_{j=1}^{N_{RL}}\eta^L_j r'^L_j\left(C^S_{SLi},T^S_S\right)\left(-\Delta H^L_{R,j}\right) \tag{8}$$

van Hasselt et al. [25] and Ojeda and Krishna [26] have reported that for countercurrent operation mode the gas phase must be included in the energy-balance equations in order to accurately simulate the heat-transfer process in the reactor because the reaction heat is distributed in two directions and there is a cooling effect of the gas phase over the liquid phase at the reactor bottom.

Initial and boundary conditions

In order to define completely the system of PDEs from mass and energy balances, it is necessary to set the initial and boundary conditions for gas, liquid, and solid phases at reactor limits in countercurrent operation mode.

(i) Initial conditions:

$$\text{For } t = 0, \text{ at } z = 0, \begin{cases} p_i^G = 0, \;\; i = H_2 \\ C_i^L = 0, \;\; i = H_2,\ LP,\ MP,\ HP, \text{ and } OP \\ C_i^L = \left(C_i^L\right)_0,\ i = TG \\ C_{SLi}^S = 0, \;\; i = H_2, \;\; TG,\ LP,\ MP,\ HP, \text{ and } OP \\ T_G = T_L = T_S^S = T_0 \end{cases} \tag{9}$$

$$\text{at } 0 < z < L_B, \begin{cases} p_i^G = 0, \;\; i = H_2 \\ C_i^L = 0,\ i = H_2,\ TG,\ LP,\ MP,\ HP, \text{ and } OP \\ C_{SLi}^S = 0,\ i = H_2,\ TG,\ LP,\ MP,\ HP, \text{ and } OP \\ T_G = T_L = T_S^S = T_0 \end{cases} \tag{10}$$

$$\text{at } z = L_B, \begin{cases} p_i^G = \left(p_i^G\right)_{L_B},\ i = H_2,\ H_2S,\ H_2O, \text{ and } CH_4 \\ C_i^L = 0,\ i = H_2,\ TG,\ LP,\ MP,\ HP, \text{ and } OP \\ C_{SLi}^S = 0,\ i = H_2,\ TG,\ LP,\ MP,\ HP, \text{ and } OP \\ T_G = T_L = T_S^S = T_0 \end{cases} \tag{11}$$

(ii) Boundary conditions:

$$\text{For } t > 0, \text{ at } z = 0, \begin{cases} C_i^L = 0,\ i = H_2,\ LP,\ MP,\ HP, \text{ and } OP \\ C_i^L = \left(C_i^L\right)_0,\ i = TG \\ C_{SLi}^S = 0,\ i = H_2,\ TG,\ LP,\ MP,\ HP, \text{ and } OP \\ T_L = \left(T_L\right)_0;\ T_S^S = \left(T_S^S\right)_0 \end{cases} \tag{12}$$

$$\text{at } z = L_B, \begin{cases} p_i^G = \left(p_i^G\right)_{L_B},\ i = H_2 \\ T_G = \left(T_G\right)_{L_B} \end{cases} \tag{13}$$

When a high-purity hydrogen stream without gas recycle is used, such as in the case of some laboratory HDT reactors (i.e., the micro-scale reactor), or when the recycled gas has been subject to purification process in industrial HDT units, the value of H_2 partial pressure ($p_{H_2}^G$) at the inlet of the catalytic bed ($z = L_B$) is equal or very close to the total operating pressure.

Integration method

The mathematical reactor model was solved numerically by applying the method of lines [27, 28]. The set of PDEs describing the heat and mass balances in the chemical reactor were transformed into a set of first-order ODEs by discretizing the spatial partial derivatives in the axial direction using the backward finite difference approximations and leaving the independent variable time (time partial derivatives) without discretize. The final system of ODEs obtained was then solved with respect to time using the adaptive Runge–Kutta pairs of various orders method. The program required to calculate thermodynamic properties, transport properties, hydrodynamic, and kinetic parameters to simultaneously solving the ODEs system was a stand-alone program coded in Fortran that can be run on a personal computer. This method gives stability in the solution of parabolic PDEs, as is the case for the model proposed in this work.

Reaction kinetic models

Anand and Sinha [12] carried out a study of direct HDC global kinetics and oligomerization of *Jatropha* oil, where the huge number of components produced inside the HDC reaction was classified using 5 lumps: estimating the reactants (TG), the light (nC_5–C_8), middle (nC_9–C_{14}), heavy (nC_{15}–C_{18}), and oligomerized ($> nC_{18}$) products, from different reaction mechanisms proposed with $CoMo/Al_2O_3$ catalyst. The four reaction product lumps as lighter (LP), middle (MP), heavy deoxygenated (HP), and oligomerized (OP) products are shown in the kinetic model A7 (Fig. 1), because this scheme was relevant for the TGs conversion modeling at temperatures > 360 °C, which is the minimum advisable temperature for this process [12, 14, 16]. The A7 kinetic model is considered a understandable process, where the four primary reactions also converts the TG to LP, MP, HP, and OP directly, followed by internal secondary cracking reactions, which additionally convert HP to MP and MP to LP.

The mild HDC reactions of TGs were simulated using the five-lump model shown in Fig. 1, which includes *Jatropha* oil (triglyceride molecules of C_{16}–C_{18}

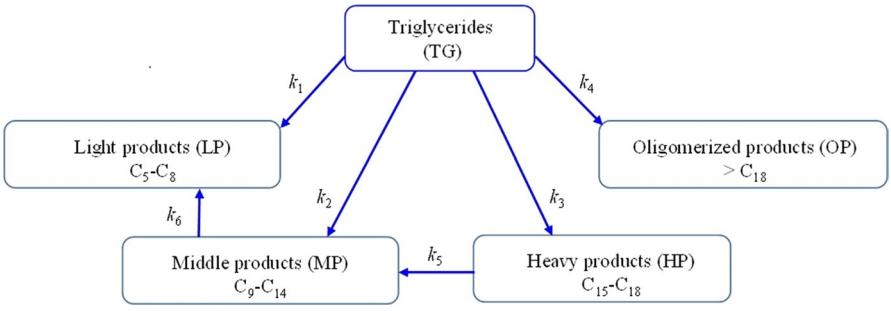

Fig. 1 Five lump kinetic model (based on the A7 model reported elsewhere [12]) for the hydroconversion of triglycerides

atoms), naphtha-range (C_5–C_8), kerosene-range (C_9–C_{14}), diesel-range (C_{15}–C_{18}), and polymerized ($> C_{18}$) hydrocarbons [29]. The reaction rates were represented by pseudo-first-order kinetic expressions as follows:

$$r_{TG}^{L} = \left(k_1 + k_2 + k_3 + k_4\right)\left(C_{SLTG}^{S}\right) \tag{14}$$

$$r_{LP}^{L} = -k_1\left(C_{SLTG}^{S}\right) - k_6\left(C_{SLMP}^{S}\right) \tag{15}$$

$$r_{MP}^{L} = -k_2\left(C_{SLTG}^{S}\right) - k_5\left(C_{SLHP}^{S}\right) + k_6\left(C_{SLMP}^{S}\right) \tag{16}$$

$$r_{HP}^{L} = -k_3\left(C_{SLTG}^{S}\right) + k_5\left(C_{SLHP}^{S}\right) \tag{17}$$

$$r_{OP}^{L} = -k_4\left(C_{SLTG}^{S}\right) \tag{18}$$

The HDC reaction rate constants were estimated by minimizing the difference between the predicted and experimental values of product yields reported by Anand and Sinha [12]. The objective function to estimate those kinetic parameters was defined as follows:

$$F = \sum_{k=1}^{N_{exp}} \sum_{i=1}^{N_{lump}} \left(w_{i,exp} - w_{i,calc}\right)_k^2 \tag{19}$$

Levenberg–Marquardt algorithm (LMA) was used and kinetic rate parameters were obtained. The estimated HDC kinetic parameters values are reported in Table 4.

Table 4 Kinetic parameters for *Jatropha* oil HDC reactions

Reaction (j)	$k_{0,j}$ (h^{-1})	$E_{a,j}$ (kJ $mol^{-1}{}_i$)	k_j (h^{-1})			$\Delta H_{R,j}^{L}$ (kJ $mol^{-1}{}_i$)
			340 °C	360 °C	380 °C	
Triglycerides (TG)	489,128.2480	52.1712	17.5798	24.2887	32.9001	− 1014
TG-LP (1)	1.1530×10^6	74.1601	0.5549	0.8785	1.3524	–
TG-MP (2)	1.7839×10^6	71.9169	1.3331	2.0815	3.1626	–
TG-HP (3)	3524.4370	27.7010	15.3911	18.2730	21.4678	–
TG-OP (4)	2.6953×10^6	72.7348	1.7156	2.6924	4.1104	–
HP-MP (5)	148.3001	40.2451	0.0553	0.0709	0.0897	− 41[a]
MP-LP (6)	1738.6270	50.6844	0.0836	0.1145	0.1538	− 41[a]

The A7 kinetic model from Anand and Sinha [12]

[a]From Tarhan [6]

Estimation of hydrodynamic and mass transfer parameters

Two flow regimes in countercurrent operation, namely trickle-flow and bubble-flow, may be useful to describe gas–liquid-solid reaction systems, however, in the current study it is assumed only trickle-flow regime in both reactor-scales (micro and industrial).

Pressure drop

The pressure drop in countercurrent flow can be represented by an equation of the Carman-Kozeny type for flow through packed beds. Below the flooding point, the following equation [30] was applied in this study:

$$\left(\frac{\Delta P}{\Delta z}\right) = \frac{8.5\mu_G a_S^2 G_G}{\rho_G} + \frac{a_S G_G^2}{\rho_G}\left(\frac{\mu_G a_S}{G_G}\right)^{0.1}\frac{1}{\in_B^3} \tag{20}$$

Under similar flow conditions, countercurrent flow presents more pressure drop than cocurrent downflow through a packed bed.

Liquid holdup

In this study the correlation of Satterfield [6] was used to estimate the liquid holdup for the micro-scale reactor:

$$\varepsilon_L = 9.9\left(Re_L\right)^{0.333}\left(Ga_L\right)^{-0.333} \tag{21}$$

For industrial scale, it can be used the correlation proposed by Otake and Okada [31] for high liquid phase Reynolds numbers (10–2000), which is given by the following expression:

$$\varepsilon_L = 6.28\left(Re_L\right)^{0.676}\left(Ga_L\right)^{-0.44} + \frac{3.8\times10^{-2}}{d_{pe}} \tag{22}$$

Wetting efficiency

Just as in TBRs with cocurrent downward operation, the uniform wetting of the catalyst particles may be a problem for a countercurrent system, particularly under trickle flow. DeMaria and White [30] correlated their experimental data in a countercurrent flow system under trickle-flow conditions by the following relationship:

$$f_w = \frac{a_w}{a_S} = 1.11\left(Re_G\right)^{-0.2}10^{-\left[0.013-0.088\left(d_{pe}/d_R\right)-3.43\times10^{-6}\left(d_{pe}/d_R\right)^{2.31}\right]Re_L} \tag{23}$$

Due to the use of powder catalyst particles and dilution with fine inert material in the micro-scale reactor, it may be assumed a complete catalyst wetting ($f_w = 1$).

The same value is used in industrial-scale reactor since criteria for complete catalyst wetting is fulfilled due usually they present high liquid mass velocities, efficient internals for a good distribution of the liquid phase and/or sufficient layer of packing to reach equilibrium liquid distribution [32].

Gas–liquid-solid mass transfer coefficients

Onda et al. [33] correlated a large amount of data in a countercurrent TBR in order to estimate the liquid-side mass transfer coefficient in concurrent operation using the equation:

$$k_i^L a_L = 0.0051\left(a_w\right)\left(\frac{g\mu_L}{\rho_L}\right)^{1/3}\left(\frac{\rho_L u_L}{a_w \mu_L}\right)^{2/3}\left(\frac{\mu_L}{\rho_L D_{Mi}^L}\right)^{-0.5}\left(a_S d_{pe}\right)^{0.4} \tag{24}$$

Here a_w is the wetted area of the solid particles. For countercurrent flow, k_i^G can be estimated with the correlation of Onda et al. [33] since it is based on an extensive amount of data:

$$k_i^G = C_d\left(a_S D_{Mi}^G\right)\left(\frac{\rho_G u_G}{a_S \mu_G}\right)^{0.7}\left(\frac{\mu_G}{\rho_G D_{Mi}^G}\right)^{1/3}\left(a_S d_{pe}\right)^{-2}$$

here

$$\begin{aligned} C_d &= 2.0 \text{ for } d_{pe} < 1.5 \text{ cm} \\ C_d &= 5.23 \text{ for } d_{pe} > 1.5 \text{ cm} \end{aligned} \tag{25}$$

The gas–liquid interphase mass transfer flux is described in terms of the two-film theory:

$$\frac{1}{K_{Li}} = \frac{RT_G Z^G}{k_i^G H_i} + \frac{1}{k_i^L} \tag{26}$$

As observed in Eq. 26, the overall external resistance to mass transfer (K_{Li}) is composed by the resistance to mass transfer in the gas (k_i^G) and liquid (k_i^L) films.

For slightly soluble gases, such as H_2, the value of the Henry's constant (H_i) is much larger than unity and then the mass transfer resistance in the gas film can be neglected [34]. Therefore, in the micro-scale reactor, as H_2 is in excess and at high purity conditions, the total mass transfer is approximately equal to the liquid side mass transfer coefficient, thus:

$$\frac{1}{K_{Li}} = \frac{1}{k_i^L} \tag{27}$$

Countercurrent-flow operation is largely used for absorption and gas–liquid reaction processes, however no information on liquid–solid mass transfer appears to have been published at this regard. According to Goto and Smith [35] gas flow

rates do not have a significant effect on the gas–liquid and liquid–solid mass-transfer coefficients in TBRs, so that the same mass-transfer coefficient values may be used for the cocurrent and countercurrent operations. Therefore, the liquid–solid mass transfer coefficient (k_i^S) can be estimated by the following empirical correlations used for cocurrent downflow operation [36]:

- For micro-scale reactor

$$\frac{k_i^S a_S}{D_{Mi}^L} = \alpha_S \left(\frac{G_L}{\mu_L}\right)^{n_S} \left(\frac{\mu_L}{\rho_L D_{Mi}^L}\right)^{1/3}$$

$$\alpha_S = -577.80 d_{pe} + 184.3$$

$$n_S = -0.5886 d_{pe} + 0.7018 \tag{28}$$

- For industrial-scale reactor

$$\frac{k_i^S}{D_{Mi}^L a_S} = 1.8 \left(\frac{G_L}{a_S \mu_L}\right)^{1/2} \left(\frac{\mu_L}{\rho_L D_{Mi}^L}\right)^{1/3} \tag{29}$$

Gas–liquid-solid heat transfer

The overall gas–liquid heat transfer coefficient can be calculated as:

$$\frac{1}{h_{GL} a_L} = \frac{1}{h_G a_L} + \frac{1}{h_L a_L} \tag{30}$$

Unfortunately, no information on heat transfer during countercurrent flow operation has been published [30]. To overcome that disadvantage the overall heat transfer coefficient ($h_{GL} a_L$) was set to 0.001.

Catalyst effectiveness factor

The catalyst effectiveness factor can be estimated as function of the Thiele modulus (ϕ). The generalized Thiele modulus for *n*th-order irreversible reaction is [34]:

$$\phi_j^L = \frac{1}{\phi_S} \left(\frac{V_p}{S_p}\right) \sqrt{\left(\frac{n+1}{2}\right) \frac{\in_S k_j \left(C_{SLi}^S\right)^{n-1}}{D_{ei}^L}} \tag{31}$$

here

$$D_{ei}^{L} = \frac{\in_S}{\tau}\left[\frac{1}{\left(\frac{1}{D_{Mi}^{L}}\right)+\left(\frac{1}{D_{Ki}^{L}}\right)}\right] \tag{32}$$

The tortuosity factor (τ) can be estimated by assuming the correlation of Weissberg [37] for randomly packed spheres:

$$\frac{1}{\tau} = \frac{\in_S}{1-\frac{1}{2}log\left(\in_S\right)} \tag{33}$$

The equivalent particle diameter (d_{pe}) and effectiveness factor (η) were estimated properly with recommended correlations [38].

Gas–liquid equilibrium

The gas–liquid solubility along the catalyst bed is represented in the mass balance equations by the Henry's law constant. To calculate the Henry's constant of gaseous solute in a solvent the following approach can be used [39]:

$$H_i = \lim_{x_i \to 0}\left(\frac{f_i^L}{x_i}\right) = \lim_{x_i \to 0}\left(P\varphi_i^L\right) \tag{34}$$

Here φ_i^L is the fugacity coefficient of gaseous compound i (solute) in the liquid phase (solvent), and its calculation is done by using the Peng-Robinson equation of state.

Ensuring ideal behaviors in TBRs

To generate reliable and consistent experimental data in a trickle-bed micro-scale HDT reactor (i.e., kinetics data), it is critical to keep the reactor operation within the desired regime, which includes plug flow of the liquid phase, complete catalyst wetting, absence of reactor wall effects, and insignificant vaporization of the liquid phase.

Criteria for plug flow

A relaxed criterion with 15% deviation from plug flow was used in our computations [40]:

$$\frac{L_B}{d_{pe}} > \frac{\sqrt{20}n}{Bo_{a,m}^{L}} ln\left[\frac{1}{\left(1-X_{TG}\right)}\right] \tag{35}$$

A value of 0.04 Bodenstein number was used in this equation since very low Reynolds' number value. Axial dispersion may influence only the results of small-scale

reactors since for industrial reactors it can be neglected. Thus, in our results, if present, axial dispersion is only affecting micro-scale reactor simulations [22]. The results of using this criterion is reported in Table 5.

Criteria for particle wetting effects

In a TBR, any partial catalyst wetting could cause bypassing of the feed and, therefore, reduce the catalyst performance. If the liquid superficial velocities are very low, which is common in a laboratory reactor because of its relatively small volume of catalyst, partial catalyst wetting can occur. It has been demonstrated analytically that if the liquid flow on catalyst particle surface is dominated by frictional forces rather than gravitational forces, the fluid will tend to spread over the catalysts uniformly. On the basis of a comparison of these forces coming from a huge amount of experimental data, Gierman [41] proposed the criterion given by Eq. 36 for even irrigation of catalyst, which has been recommended and used by a number of researchers [40, 42]. Table 5 reports the results for application of this criterion.

$$W = \frac{\mu_L u_L}{\rho_L d_{pe}^2 g} > 5.0 \times 10^{-6} \tag{36}$$

Criteria for wall effects

Normally, reactor wall effects on reactor performance are not a concern for an industrial HDT reactor, because the reactor diameter is much larger than the catalyst particle size. In this study, the calculated ratio value for the cocurrent micro-reactor used to obtain the kinetics data is shown in Table 5.

Criterion for liquid vaporization

In order to ensure that at both operation modes, concurrent and countercurrent micro-reactor, which was used for validation [14], there are not effects by partial vaporization of the liquid phase, the criterion of Hanika et al. was applied [43] to assess the significance of liquid vaporization in a TBR.

$$\frac{\rho_L u_L MW_L}{\rho_G u_G MW_G} < \frac{P_v(T_L)}{P - P_v(T_L)} \tag{37}$$

The results obtained by applying this criterion at both micro- and industrial-scale reactors are shown in Table 5.

Table 5 Criteria results to ensure ideal behaviors in TBRs

Condition	Criterion	Micro scale[a]		Industrial scale	
		LHS	RHS	LHS	RHS
Plug flow	$\frac{L_B}{d_{pe}} \geq 30 - 350$	77.3	30	3360	350
	Fulfilled?	Yes		Yes	
	$\frac{L_B}{d_{pe}} \geq \frac{20n}{Bo^L_{a,m}} ln\left[\frac{1}{(1-X_{TG})}\right]$	77.3	4590[b]	3360	912[d]
	Fulfilled?	No		Yes	
	$\frac{L_B}{d_{pe}} \geq \frac{\sqrt{20n}}{Bo^L_{a,m}} ln\left[\frac{1}{(1-X_{TG})}\right]$	77.3	436[c]	3360	204[d]
	Fulfilled?	No		Yes	
	Conclusions	Back-mixing can occur		No axial dispersion	
Wetting effects	$W = \frac{\mu_L u_L}{\rho_L d_{pe}^2 g} \geq 5.0 \times 10^{-6}$	4.4×10^{-6}	5.0×10^{-6}	9.0×10^{-6}	5.0×10^{-6}
	Fulfilled?	No (but close results)		Yes	
	Conclusions	Fair catalyst wetting		Good catalyst wetting	
Wall effects	$\frac{d_R}{d_{pe}} \geq 25$	36	25	1200	25
	Fulfilled?	Yes		Yes	
	$\frac{d_{pe}}{d_{pi}} \leq 10$	1.4	10	∞	10
	Fulfilled?	Yes		Not apply	
	Conclusions	Non preferential flow		Non preferential flow	
Vaporization effects	$\frac{\rho_L u_L MW_G}{\rho_G u_G MW_L} < \frac{P_v(T_L)}{P - P_v(T_L)}$	0.009737	0.009313	0.009738	0.009313
	Fulfilled?	No		No	
	Conclusions	Negligible liquid vaporization		Negligible liquid vaporization	

Micro- and industrial-scale TBR in cocurrent and countercurrent operation mode, respectively, LHS = left-hand side, RHS = right-hand side, operating conditions: T = 380 °C, P = 8 MPag, LHSV = 8.0 h^{-1} for micro scale reactor and 2.66 h^{-1} for industrial scale reactor, H_2/feed ratio = 1500 NL L^{-1}

[a] $d_{pe} = d_{pi}$ because hydrodynamics is influenced by the smaller particles

[b] with $Bo^L_{a,m}$ by Hochman-Effron correlation [6]

[c] with $Bo^L_{a,m} = 0.04$ [40]

[d] with $Bo^L_{a,m}$ by Michell-Furzer correlation [30]

Results and discussion

The three-phase isothermal reactor model developed in this work was applied to simulate and analyze the dynamic performance of a countercurrent micro-scale reactor reported elsewhere [14]. The model solution for such countercurrent micro-reactor is an initial-value problem as the concentrations of the reactants and products are known previously at the reactor inlet.

Dynamic simulation of micro-scale reactor for validation

In Table 5 the results of criteria used to ensure ideal reactor behavior are reported. As can be seen, wall effects and liquid vaporization were negligible for both scales while wetting effects were complete only for industrial reactor while at smaller scale, the results were not satisfactory. If the simpler criterion is used, plug flow is ensured at both reactor scales. Wetting effects could affect experimental reactor performance due to incomplete catalyst wetting.

Since the cocurrent micro-scale reactor used to obtain the experimental data was operated within almost ideal behavior [12], the kinetic parameters estimated can be assumed without mass transfer resistance effects, which allows them to be used for modeling at any other reactor scale with different operation modes: cocurrent, countercurrent, upflow cocurrent, etc. Under this consideration, an earlier model reported by Forghani et al. [14], who modeled a countercurrent micro-scale TBR for triglyceride hydrocracking but at steady-state conditions, was used to validate our dynamic model when it reaches the steady-state in order to be able to compare in both cases the concentration and partial pressures profiles obtained along the reactor.

Fig. 2 depicts the dynamic simulated liquid molar concentration profiles of TGs along the experimental catalyst bed [14] at several times ranging from 60 to 600 s. The concentration profiles at different times were generated from the mathematical model of a countercurrent micro-scale reactor at a temperature of 380 °C, pressure of 8 MPag, LHSV of 8.0 h^{-1}, and H_2/feed ratio of 1500 NL L^{-1}. At short time (i.e., 60 s) the feed only reaches 50% of the total reactor length that is why the TGs content in the remaining 50% of the reactor length is zero, which means that this part of the reactor is empty of reacting mixture. As the time passes, the reactor is completely filled with the liquid reacting mixture, reaching the steady-state condition near 600 s. At that time, the comparison of concentration between predicted TG concentration and that experimental reported [14], are in good agreement. Other dynamic profiles of small-scale reactor were obtained (not shown) and it was observed also close agreement between results our model and those obtained by [14], including well prediction of concentration of experimental LP.

The variation of the hydrogen partial pressure in the gaseous phase and the concentration in the liquid phase along the catalyst bed are shown in Fig. 3a and b, at times very close to the beginning of the operation (60 s), intermediate times (100, 200, and 300 s), and when the steady-state is reached (600 s).

In Fig. 3a, it is observed that because of the high gas velocity inside the micro-scale reactor the curves of hydrogen partial pressure at 300 and 600 s almost overlap. The overall shape of molar concentration and partial pressure profiles of H_2 are determined by balance between the reaction rate and mass transfer. Since in countercurrent operation mode the H_2 phase is fed at the bottom of the reactor, its consumption trend is opposite to that observed in cocurrent mode of operation (i.e., partial pressure decreases from the bottom to the top of the reactor). The H_2 concentration in the liquid phase increases rapidly at the beginning of the catalytic bed because of the high gas–liquid mass transfer in this zone as expected (Fig. 3b).

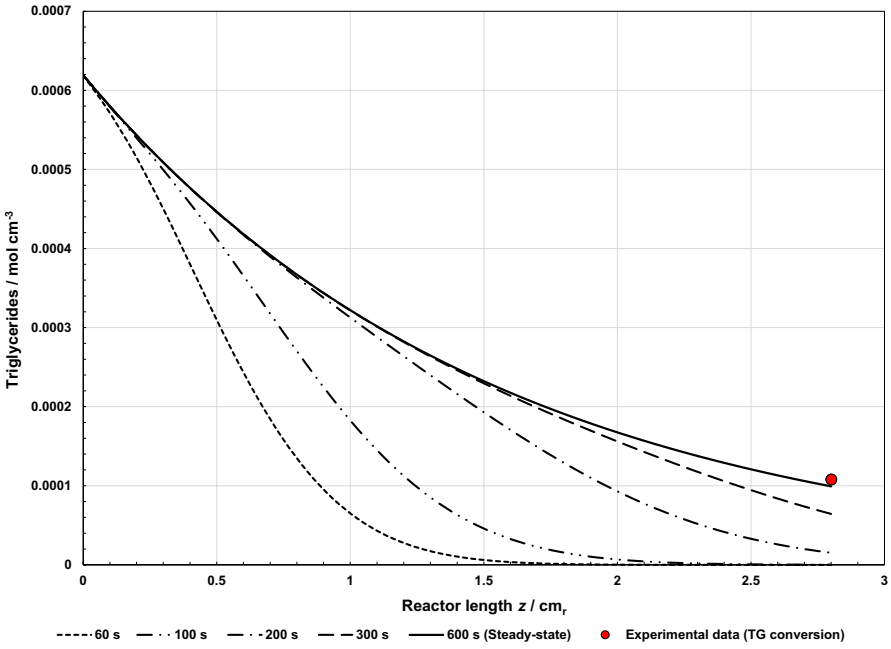

Fig. 2 Simulation of evolution profiles of triglycerides concentration in the liquid phase down through the catalyst bed of the countercurrent micro-scale reactor as a function of time. Reaction conditions: 380 °C, 8 MPag, LHSV of 8.0 h^{-1}, and 1500 NL L^{-1} of H_2/Oil volume ratio. Predicted profiles of concentrations at different times: (*dotted line*) 60 s, (*hyphen double mid dot hyphen line*) 100 s, (*hyphen single mid dot hyphen line*) 200 s, (*dashed line*) 300 s, (*solid line*) 600 s; and experimental data (*circle symbol*). Lines represent solved mass balance equation (Eq. 3)

Dynamic simulation of industrial-scale reactor for scale-up

After the model was validated to reproduce the performance of the countercurrent micro-scale reactor, it was applied to predict the expected behavior of a commercial HDT catalyst in an industrial unit. The industrial-scale reactor information was taken from a design data book and from usual operating conditions [44], as described in Table 3. Industrial HPR TBRs are normally considered to operate under adiabatic conditions because energy losses from the reactor are usually negligible compared to the energy generated by the reaction [45], and also by security reasons.

For 99.99% conversion a maximum temperature gradient across the catalyst bed of 370 K was obtained, in agreement to Anand et al. [17]. Assuming adiabatic conditions, the heat of reaction $\Delta H^{L}_{R,TG}$ can be estimated from Eq. 38 as follows [32, 46]:

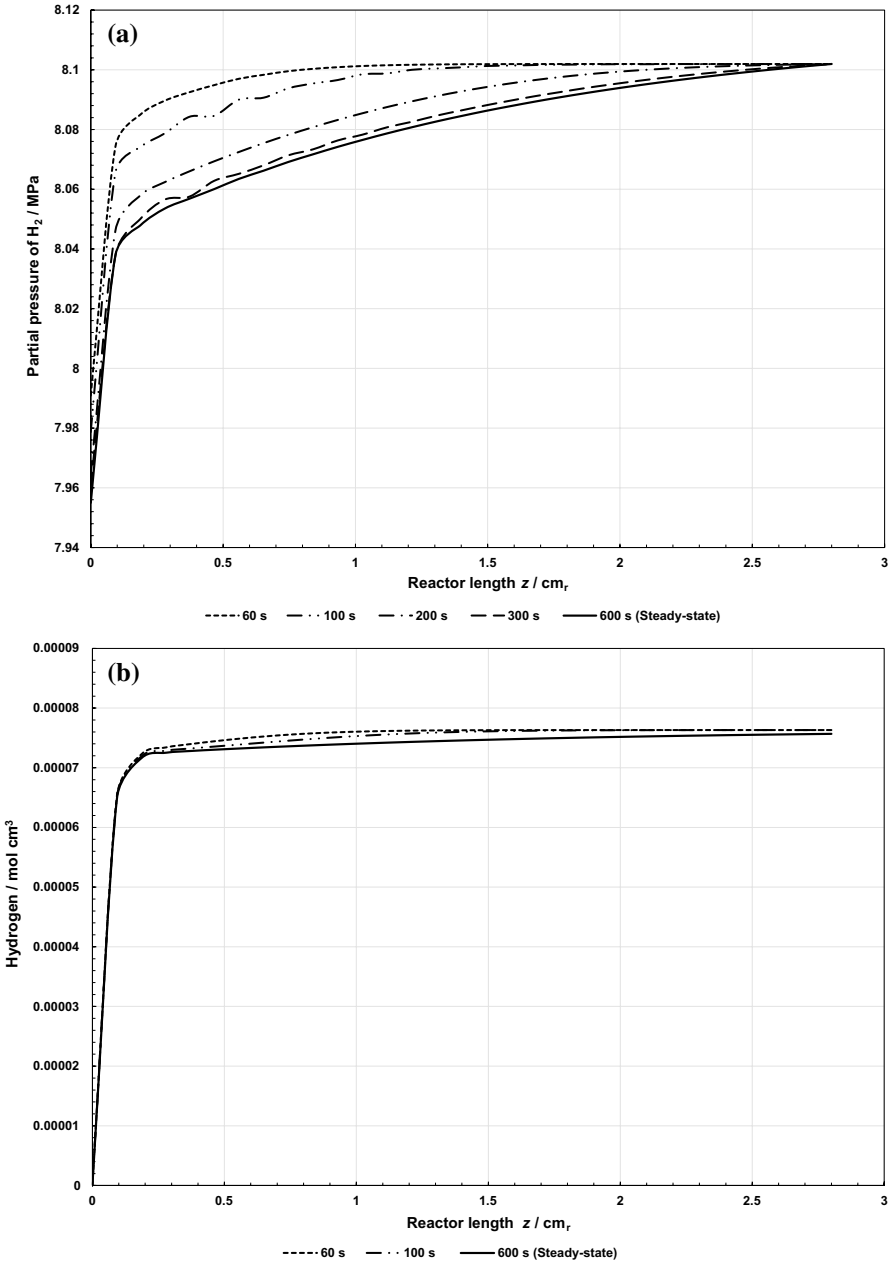

Fig. 3 Simulation of evolution profiles of **a** hydrogen partial pressures and **b** hydrogen liquid concentrations, both down through the catalytic bed of the countercurrent micro-scale reactor. Reaction conditions: 380 °C, 8.0 MPag, LHSV of 8.0 h^{-1}, and 1500 NL L^{-1} of H_2/Oil volume ratio. Predicted profiles of partial pressures and concentrations at different times: (*dotted line*) 60 s, (*hyphen double mid dot hyphen line*) 100 s, (*hyphen single mid dot hyphen line*) 200 s, (*dashed line*) 300 s, (*solid line*) 600 s. Lines represent solved mass balance equations (Eqs. 1 and 2)

$$-\Delta H_{R,TG}^{L}=\frac{\left(\Delta T_{ad}\right)\left(\rho_{L}\right)_{0}\left(Cp_{L}\right)_{0}}{\left(X_{TG}\right)\left(C_{TG}^{L}\right)_{0}}$$
$$=\frac{(370K)\left(0.579982\ \mathrm{g}_{L}\mathrm{cm}_{L}^{-3}\right)\left(2.907417\ \mathrm{Jg}_{L}^{-1}\mathrm{K}^{-1}\right)}{(0.9999)\left(6.190819\times10^{-4}\ \mathrm{mol}_{TG}\ \mathrm{cm}_{L}^{-3}\right)}=1.00810^{6}\ \mathrm{Jmol}_{TG}^{-1} \tag{38}$$

In Fig. 4, it is demonstrated that the adiabatic temperature rise for different values of the heat of reaction. It is also shown, from this figure, that the estimated heat of reaction of 1014 kJ mol^{-1} for a maximum temperature gradient of 370 K is near to the value of total reaction heat of 1189 kJ mol^{-1} reported by Anand et al. [17] for HPR of *Jatropha* oil. The heat of reaction calculated by Eq. 38 is slightly lower than its estimated value by simulation of 1014 kJ mol^{-1} because this equation is only for adiabatic TBRs in cocurrent operation mode, which does not take into account the cooling effect of the gas phase over the liquid phase at the bottom of the reactor for a countercurrent flow. This effect can be observed in Fig. 5.

Fig. 5 shows the evolution of gas, liquid, and solid phase temperature along the reactor for countercurrent operation mode. It may be observed that the liquid and solid phase temperature profiles overlap, because the maximum temperature gradient between them is almost negligible ($\Delta T_{L\text{-}S}$ = 2.25 °C).

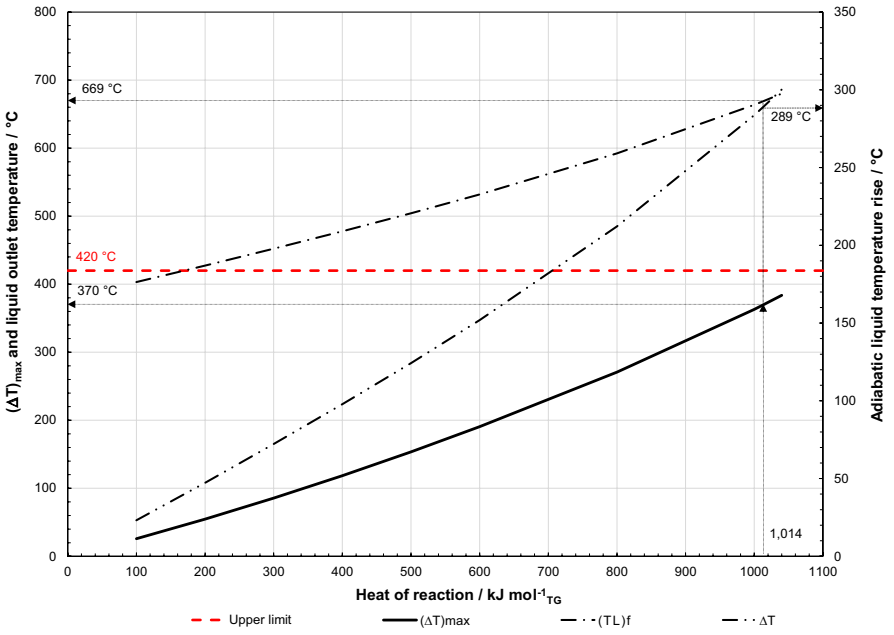

Fig. 4 Effect of the reaction heat on the liquid phase temperature in the industrial scale reactor at steady-state. Predicted data: (*dashed line*) upper limit for the catalyst operating temperature, (*solid line*) maximum temperature gradient reached in the catalyst bed, (*hyphen single mid dot hyphen line*) liquid phase temperature at the reactor outlet, (*hyphen double mid dot hyphen line*) liquid phase temperature gradient between the reactor inlet and outlet conditions. Lines represent solved energy balance equation (Eq. 7)

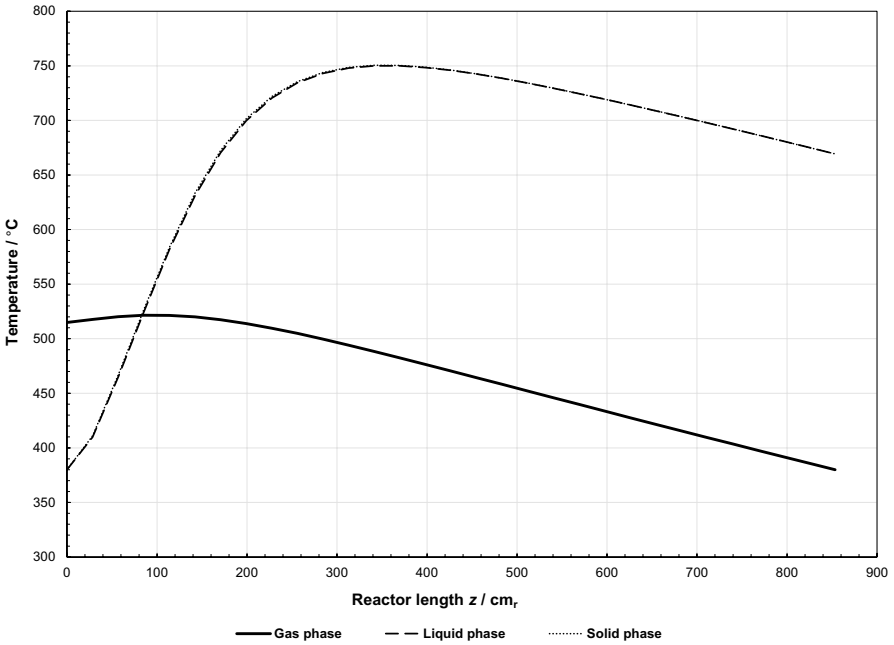

Fig. 5 Simulation of evolution profiles of temperature along the catalytic bed of the gas, liquid, and solid phases in the countercurrent industrial-scale reactor at steady-state. Reaction conditions: 380 °C, 8 MPag, 2.66 h^{-1} of LHSV, and 1500 NL L^{-1} of H_2/Oil volume ratio. Predicted temperature profiles for the three phases present in the industrial-scale catalytic bed: (*solid line*) gas phase, (*dashed line*) liquid phase, (*dotted line*) solid phase. Lines represent solved energy balance equations (Eqs. 6–8)

Before analyzing the results from the dynamic simulation of the HDT reactor, it is advisable firstly, to understand the limits imposed by the own process over the reactor inner temperature. One possible way to set this limit is through the criterion of runaway, which determines the maximum temperature before the generation of hot-spots in catalytic fixed-bed reactors, according to the reaction kinetics. By applying Eq. 39 the maximum temperature allowed for the kinetic data of global HDC reaction of TGs shown in Table 4 can be calculated [8, 34].

$$T_M = \frac{1}{2}\left[\frac{E_{a,TG}}{R} - \sqrt{\frac{E_{a,TG}}{R}\left(\frac{E_{a,TG}}{R} - 4T_L\right)}\right] \tag{39}$$

Substituting the kinetic data in Eq. 39, a maximum allowable temperature of 741 K (467 °C) is obtained which is the upper limit to avoid hot-spots and reactor runaway; however, it is also necessary to take into account the metallurgical constraints of the reactor material.

Fig. 6 exhibit the predicted dynamic liquid molar concentration profiles of TGs along the industrial catalytic bed at different times ranging from 60 to 1700 s for an inlet reactor temperature of 380 °C. The dynamic simulation was carried out at the same reaction conditions than those used for the simulation of the

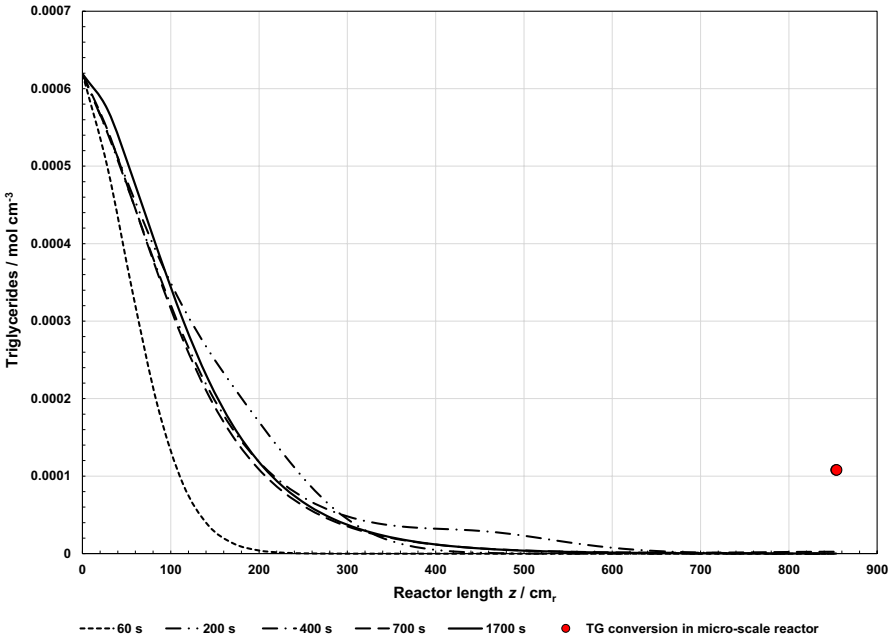

Fig. 6 Simulation of evolution profiles of triglycerides concentration in the liquid phase down through the catalyst bed of the countercurrent industrial-scale reactor as a function of time. Reaction conditions: 380 °C, 8 MPag, LHSV of 2.66 h^{-1}, and 1500 NL L^{-1} of H_2/Oil volume ratio. Predicted profiles of concentrations at different times: (*dotted line*) 60 s, (*hyphen double mid dot hyphen line*) 200 s, (*hyphen single mid dot hyphen line*) 400 s, (*dashed line*) 700 s, (*solid line*) 1700 s; and experimental data (*circle symbol*). Lines represent solved mass balance equation (Eq. 3)

countercurrent micro-scale reactor except for the LHSV (see Table 3). The value of TGs concentration reported at the exit of the isothermal micro-scale reactor is included in this figure (red circle) for comparison. The micro-scale experimental TGs concentration value was higher than that predicted for the industrial-scale reactor because of the adiabatic temperature rise observed in the liquid phase at the first half of the industrial reactor.

Parts a and b of Fig. 7 illustrate the dynamic profiles of TGs concentration and liquid phase temperature of industrial HDT reactor, respectively, which were calculated with the mass and energy balance equations (Eqs. 1–8). The results of the transient simulation of TGs concentration and experimental temperature profiles for the countercurrent micro-scale reactor are also shown for comparison (solid lines). It can be observed that the steady-state in the micro-scale reactor is reached faster in comparison with the industrial reactor. This is not surprising because the operating condition of LHSV in the micro-scale reactor is particularly greater. There are some differences in the TGs concentration profiles at certain period of time before the steady-state operation is reached in micro- and industrial-scales reactor, which can be attributed to the constant temperature in the former and the adiabatic temperature increase in the latter.

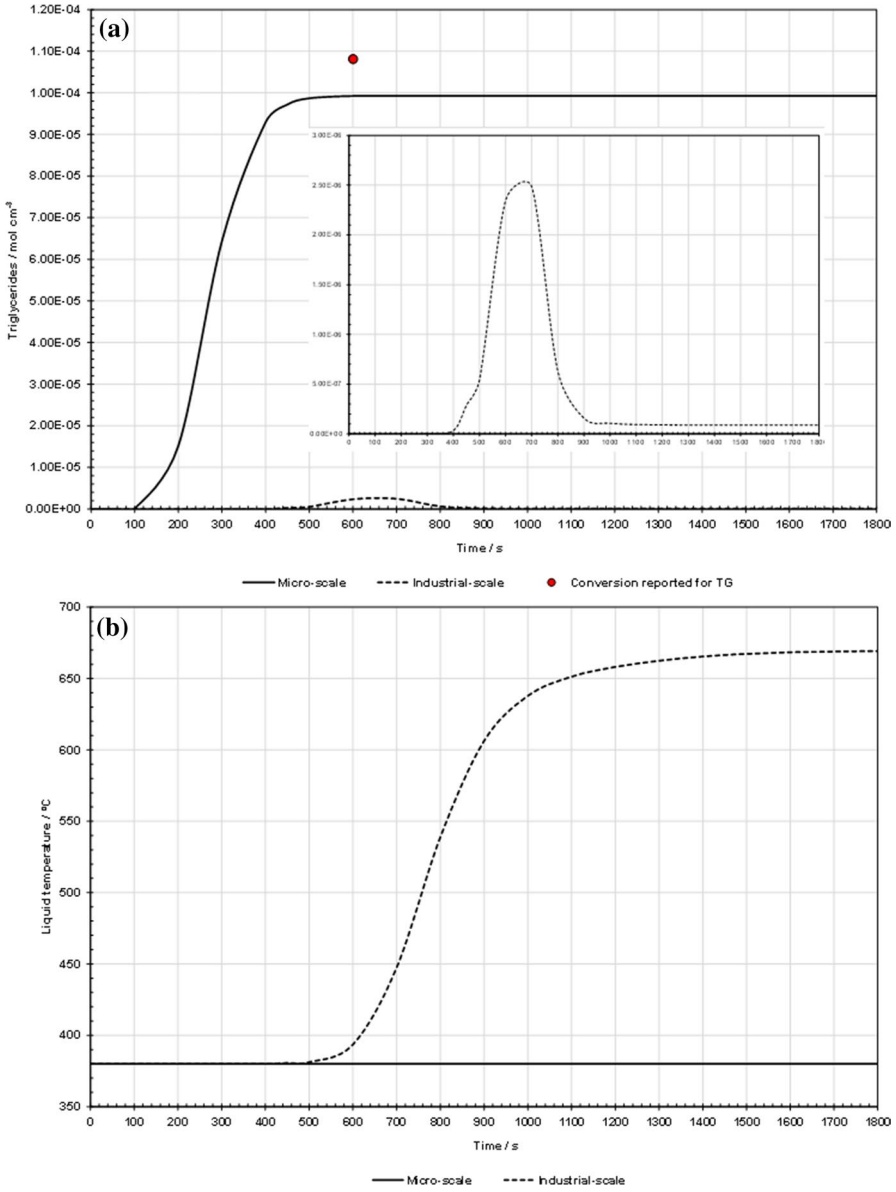

Fig. 7 Simulation of **a** triglycerides concentration and **b** liquid-phase temperature as a function of time at the bottom of both countercurrent micro- and industrial-scale reactors. Reaction conditions: 380 °C, 8 MPag, LHSV of 8.0 h^{-1} for micro-scale reactor and 2.66 h^{-1} for industrial-scale reactor, and 1500 NL L^{-1} of H_2/Oil volume ratio. Predicted dynamic profiles of triglycerides concentration and liquid phase temperature at the outlet of each reactor scale: (*solid line*) micro-scale reactor, (*dashed line*) industrial-scale reactor; and experimental data (*circle symbol*). Lines represent solved mass balance equation (Eq. 3) and energy balance equation (Eq. 7)

Fig. 7a also shows how TGs content in the product at the exit of the two scale reactors changes as a function of time, and it is possible to observe that a small amount of hydrocracked product is detected at the exit of the micro-scale reactor at about 105 s (1.74 min) and in the industrial-scale reactor at about 376 s (6.3 min), which correspond to the mean residence time given by the interstitial velocity.

After the actual residence time in each catalytic bed is attained, concentrations start increasing and finally the steady-state is reached at *ca.* 600 s (10 min) and ~ 1700 s (28.3 min) in the micro- and industrial-scale reactor, respectively.

The dynamic predicted axial profiles of the liquid phase temperature in the industrial reactor at different times are presented in the Fig. 8. In this figure the catalyst temperature profile is not shown, because as reported before, the maximum difference of temperature between the liquid and solid phase was of only 2.25 °C. This figure also demonstrates that the rise in reaction temperature is higher in the initial part of the industrial reactor, due to the greater hydroconversion of TGs occurring in this zone. The phenomenon called "wrong-way" behavior was not found at the beginning of the reactor as reported elsewhere [24]. This can be attributed to the fast and high conversion of TGs in the first half of the catalyst bed, in such a way that there is not enough reactant in the latter half of the reactor that can lead to a transient temperature decrease.

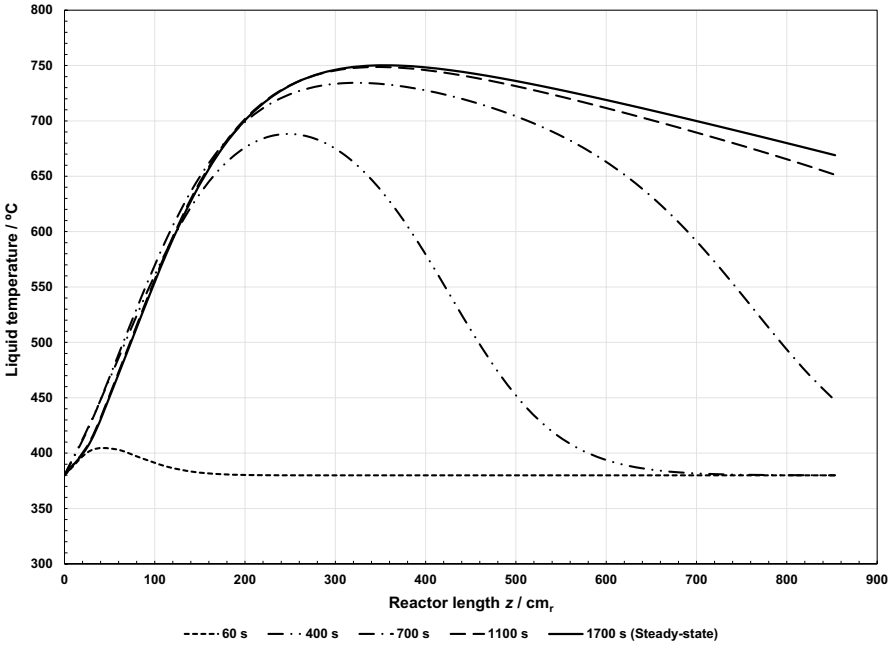

Fig. 8 Simulated temperature profiles of the liquid phase down through the catalyst bed of the countercurrent industrial-scale reactor with time. Reaction conditions: 380 °C, 8 MPag, LHSV of 2.66 h^{-1}, and 1500 NL L^{-1} of H_2/Oil volume ratio. Predicted liquid phase temperature profiles at different times: (*dotted line*) 60 s, (*hyphen double mid dot hyphen line*) 400 s, (*hyphen single mid dot hyphen line*) 700 s, (*dashed line*) 1100 s, (*solid line*) 1700 s. Lines represent solved energy balance equation (Eq. 7)

In order to simulate the effect of commercial size catalyst particles, the effectiveness factors were estimated based on chemical structures of the reactant compounds and arrived from correlations given earlier. Fig. 9 shows the transient behavior of the effectiveness factor for the global HDC reaction of TGs, assuming a typical first order reaction, at different positions in the catalyst bed. It is shown the advantage with the countercurrent operation mode by the cooling effect of the gas phase, since from the bed position of 340 cm and beyond in the catalytic bed, the effectiveness factor starts to increase because the rate of diffusion becomes higher than the reaction rate and then the effectiveness factor value increases along the remaining catalyst bed.

At industrial scale, the liquid-phase temperature increases along the first half of the HDT reactor due to the adiabatic operation mode and to the exothermic nature of the reactions, resulting in a decrease of the effectiveness factors because the reaction rates increase. However, in the last half of the reactor, the liquid-phase temperature decreases due to the cooling effect of the gas-phase entering at the bottom of the reactor with a lower temperature undergoing a slight increase of the effectiveness

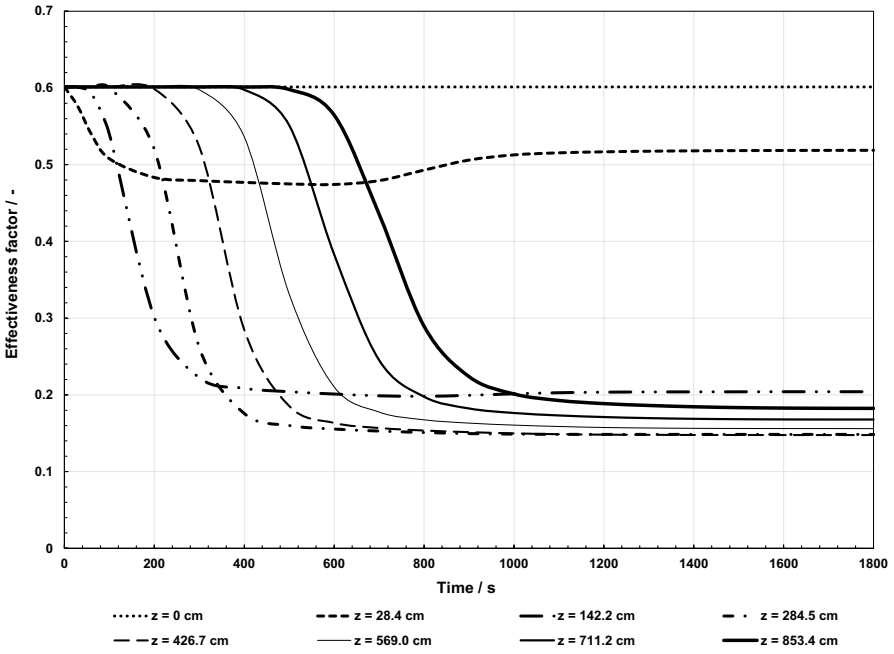

Fig. 9 Simulation of transient effectiveness factor for the overall HDC reaction of TGs in the countercurrent industrial-scale reactor at different catalytic bed positions. Reaction conditions: 380 °C, 8 MPag, LHSV of 2.66 h^{-1}, and 1500 NL L^{-1} of H_2/Oil volume ratio. Predicted profiles of the effectiveness factor for triglycerides HDC reactions at different catalytic bed positions: (*round dotted line*) 0 cm, (*square dotted line*) 28.4 cm, (*hyphen double mid dot hyphen line*) 142.2 cm, (*hyphen single mid dot hyphen line*) 284.5 cm, (*dashed line*) 426.7 cm, (*thin solid line*) 569 cm, (*solid line*) 711.2 cm, (*thick solid line*) 853.4 cm. Lines represent solved catalyst effectiveness factor equations (Eqs. 31–33)

factors because the reaction rates decrease as shown at steady-state conditions in Fig. 9.

Conclusions

A TBR model for successfully simulating the dynamic behavior with countercurrent operation mode of micro-scale and industrial-scale reactors for hydrocracking of vegetable oils was developed in this work. Among relevant findings, the model predicts at industrial-scale the highest conversion of TGs to green diesel along the first half of the catalytic bed due major gradients in temperature and reagents in this zone and also increasing effectiveness factor after second mid part of catalytic bed due effect of cooling reactor mixture by gas phase since as it ascends avoids higher reactor temperatures.

The proposed dynamic model can be used as a tool to estimate kinetic, hydrodynamic, and thermodynamic parameters, for scale-up and design of new HDO reactors, and for further research in the production of renewable or green fuels.

Acknowledgements The authors thank Instituto Politécnico Nacional (IPN)—México for its financial support to this research Project (SIP-20200787).

Compliance with ethical standards

Conflict of interest The authors declare that they have no conflict of interest.

References

1. Kubičková I, Kubička D (2010) Utilization of triglycerides and related feedstocks for production of clean hydrocarbon fuels and petrochemicals: a review. Waste Biomass Valoriz 1(3):293–308. https://doi.org/10.1007/s12649-010-9032-8
2. Liu Y, Sotelo-Boyás R, Murata K, Minowa T, Sakanishi K (2011) Hydrotreatment of vegetable oils to produce bio-hydrogenated diesel and liquefied petroleum gas fuel over catalysts containing sulfided Ni–Mo and solid acids. Energy Fuels 25(10):4675–4685. https://doi.org/10.1021/ef200889e
3. Kubička D, Šimáček P, Žilková N (2009) Transformation of vegetable oils into hydrocarbons over mesoporous-alumina-supported CoMo catalysts. Top Catal 52(1–2):161–168. https://doi.org/10.1007/s11244-008-9145-5
4. Stumborg M, Wong A, Hogan E (1996) Hydroprocessed vegetable oils for diesel fuel improvement. Bioresour Technol 56(1):13–18. https://doi.org/10.1016/0960-8524(95)00181-6
5. Huber GW, O'Connor P, Corma A (2007) Processing biomass in conventional oil refineries: production of high quality diesel by hydrotreating vegetable oils in heavy vacuum oil mixtures. Appl Catal A 329(1):120–129. https://doi.org/10.1016/j.apcata.2007.07.002
6. Tarhan MO (1983) Catalytic reactor design. McGraw-Hill, New York
7. García-Dávila J, Ocaranza-Sánchez E, Rojas-López M, Muñoz-Arroyo JA, Ramírez J, Martínez-Ayala AL (2014) *Jatropha curcas* L. oil hydroconversion over hydrodesulfurization catalysts for biofuel production. Fuel 135(1):380–386. https://doi.org/10.1016/j.fuel.2014.07.006
8. Mendoza-Sepúlveda CC (2012) Simulación CFD de la transferencia de calor en un reactor de hidrotratamiento de aceites vegetales de segunda generación. M.Sc. Thesis (in spanish), Universidad Nacional de Colombia, Sede Medellín, Colombia
9. Charusiri W, Vitidsant T (2005) Kinetic study of used vegetable oil to liquid fuels over sulfated zirconia. Energy Fuels 19(5):1783–1789. https://doi.org/10.1021/ef0500181

10. Sebos I, Matsoukas A, Apostolopoulos V, Papayannakos N (2009) Catalytic hydroprocessing of cottonseed oil in petroleum diesel mixtures for production of renewable diesel. Fuel 88(1):145–149. https://doi.org/10.1016/j.fuel.2008.07.032
11. Templis C, Vonortas A, Sebos I, Papayannakos N (2011) Vegetable oil effect on gasoil HDS in their catalytic co-hydroprocessing. Appl Catal B 104(1):324–329. https://doi.org/10.1016/j.apcatb.2011.03.012
12. Anand M, Sinha AK (2012) Temperature-dependent reaction pathways for the anomalous hydrocracking of triglycerides in the presence of sulfided Co–Mo–catalyst. Bioresour Technol 126(1):148–155. https://doi.org/10.1016/j.biortech.2012.08.105
13. Sharma RK, Anand M, Rana BS, Kumar R, Farooqui SA, Sibi MG, Sinha AK (2012) *Jatropha*-oil conversion to liquid hydrocarbon fuels using mesoporous titanosilicate supported sulfide catalysts. Catal Today 198(1):314–320. https://doi.org/10.1016/j.cattod.2012.05.036
14. Forghani AA, Jafarian M, Pendleton P, Lewis DM (2014) Mathematical modelling of a hydrocracking reactor for triglyceride conversion to biofuel: model establishment and validation. Int J Energy Res 38(12):1624–1634. https://doi.org/10.1002/er.3244
15. Attanatho L (2012) Performances and kinetic studies of hydrotreating of bio-oils in microreactor. Ph.D. Thesis, Oregon State University, Corvallis, Oregon
16. Kumar R, Rana BS, Tiwari R, Verma D, Kumar R, Joshi RK, Garg MO, Sinha AK (2010) Hydroprocessing of *Jatropha* oil and its mixtures with gas oil. Green Chem 12(1):2232–2239. https://doi.org/10.1039/c0gc00204f
17. Anand M, Farooqui SA, Kumar R, Joshi R, Kumar R, Sibi MG, Singh H, Sinha AK (2016) Kinetics, thermodynamics and mechanisms for hydroprocessing of renewable oils. Appl Catal A 516(1):144–152. https://doi.org/10.1016/j.apcata.2016.02.027
18. Jain S, Sharma MP (2010) Prospects of biodiesel from *Jatropha* in India: a review. Renew Sustain Energy Rev 14(2):763–771. https://doi.org/10.1016/j.rser.2009.10.005
19. Sarma AK, Kumar P, Aslam M, Chouhan APS (2014) Preparation and characterization of *Musa balbisiana* Colla underground stem nano-material for biodiesel production under elevated conditions. Catal Lett 144(7):1344–1353. https://doi.org/10.1007/s10562-014-1206-8
20. Achten WMJ, Verchot L, Franken YJ, Mathijs E, Sing VP, Aerts R, Muys B (2008) *Jatropha* biodiesel production and use. Biomass Bioenergy 32(12):1063–1084. https://doi.org/10.1016/j.biombioe.2008.03.003
21. Ramírez LF, Escobar J, Galván E, Vaca H, Murrieta FR, Luna MRS (2004) Evaluation of diluted and undiluted trickle-bed hydrotreating reactor with different catalyst volume. Petrol Sci Technol 22(1–2):157–175. https://doi.org/10.1081/LFT-120028530
22. Mederos FS, Ancheyta J (2007) Mathematical modeling and simulation of hydrotreating reactors: cocurrent versus countercurrent operations. Appl Catal A 332(1):8–21. https://doi.org/10.1016/j.apcata.2007.07.028
23. Bellos GD, Papayannakos NG (2003) The use of a three phase microreactor to investigate HDS kinetics. Catal Today 79–80(1):349–355. https://doi.org/10.1016/S0920-5861(03)00062-2
24. Mederos FS, Ancheyta J, Elizalde I (2012) Dynamic modeling and simulation of hydrotreating of gas oil obtained from heavy crude oil. Appl Catal A 425–426(1):13–27. https://doi.org/10.1016/j.apcata.2012.02.034
25. van Hasselt BW, Lebens PJM, Calis HPA, Kapteijn F, Sie ST, Moulijn JA, van den Bleek CM (1999) A numerical comparison of alternative three-phase reactors with a conventional trickle-bed reactor. The advantages of countercurrent flow for hydrodesulfurization. Chem Eng Sci 54(21):4791–1499. https://doi.org/10.1016/S0009-2509(99)00196-7
26. Ojeda-Nava JA, Krishna R (2004) In-situ stripping of H_2S in gasoil hydrodesulphurization–reactor design considerations. Chem Eng Res Des 82(2):208–214. https://doi.org/10.1205/026387604772992783
27. Walas SM (1991) Modeling with differential equations in chemical engineering. Butterworth-Heinemann, Boston
28. Schiesser WE (1991) The numerical method of lines–integration of partial differential equations. Academic Press, San Diego
29. Sinha AK, Anand M, Rana BS, Kumar R, Farooqui SA, Sibi MG, Kumar R, Joshi RK (2013) Development of hydroprocessing route to transportation fuels from non-edible plant-oils. Catal Surv Asia 17(1):1–13. https://doi.org/10.1007/s10563-012-9148-x
30. Shah YT (1979) Gas-liquid-solid reactor design. McGraw-Hill, New York

31. Otake T, Okada K (1953) Liquid holdup in packed towers—operating holdup without gas flow. Kagaku Kogaku 17(5):176–184. https://doi.org/10.1252/kakoronbunshu1953.17.176
32. Kubička D, Tukač V (2013) Hydrotreating of triglyceride-based feedstocks in refineries. In: Murzin DY (ed) Advances in chemical engineering. Chemical engineering for renewables conversion. Academic Press, San Diego, pp 141–194. https://doi.org/10.1016/B978-0-12-386505-2.00003-1
33. Onda K, Takeuchi H, Okumoto Y (1968) Mass transfer coefficients between gas and liquid phases in packed columns. J Chem Eng Jpn 1(1):56–62. https://doi.org/10.1252/jcej.1.56
34. Froment GF, Bischoff KB (1990) Chemical reactor analysis and design. Wiley, New York
35. Goto S, Smith JM (1978) Performance of slurry and trickle-bed reactors: application to sulfur dioxide remova. AIChE J 24(2):286–293. https://doi.org/10.1002/aic.690240218
36. Goto S, Smith JM (1975) Trickle-bed reactor performance. Part I. Holdup and mass transfer effects. AIChE J 21(4):706–713. https://doi.org/10.1002/aic.690210410
37. Weissberg HL (1963) Effective diffusion coefficient in porous media. J Appl Phys 34:2636–2639. https://doi.org/10.1063/1.1729783
38. Mederos FS, Elizalde I, Ancheyta J (2009) Steady-state and dynamic reactor models for hydrotreatment of oil fractions: a review. Catal Rev 51(4):485–607. https://doi.org/10.1080/01614940903048612
39. Moysan JM, Huron MJ, Paradowski H, Vidal J (1983) Prediction of the solubility of hydrogen in hydrocarbon solvents through cubic equations of state. Chem Eng Sci 38(7):1085–1092. https://doi.org/10.1016/0009-2509(83)80029-3
40. Mederos FS, Ancheyta J, Chen J (2009) Review on criteria to ensure ideal behaviors in trickle-bed reactors. Appl Catal A 355(1–2):1–19. https://doi.org/10.1016/j.apcata.2008.11.018
41. Gierman H (1988) Design of laboratory hydrotreating reactors scaling down of trickle-flow reactors. Appl Catal 43(2):277–286. https://doi.org/10.1016/S0166-9834(00)82732-3
42. Mary G, Chaouki J, Luck F (2009) Trickle-bed laboratory reactors for kinetic studies. Int J Chem React Eng 7(1):1–60. https://doi.org/10.2202/1542-6580.1730
43. Hanika J, Sporka K, Ruzicka V, Hrstka J (1976) Measurement of axial temperature profiles in an adiabatic trickle bed reactor. Chem Eng J 12(3):193–197. https://doi.org/10.1016/0300-9467(76)87012-8
44. Rodríguez MA, Ancheyta J (2004) Modeling of hydrodesulfurization (HDS), hydrodenitrogenation (HDN), and the hydrogenation of aromatics (HDA) in a vacuum gas oil hydrotreater. Energy Fuels 18(3):789–794. https://doi.org/10.1021/ef030172s
45. Shah YT, Paraskos JA (1975) Criteria for axial dispersion effects in adiabatic trickle bed hydroprocessing reactors. Chem Eng Sci 30(9):1169–1176. https://doi.org/10.1016/0009-2509(75)87020-5
46. Valerius G, Zhu X, Hofmann H, Arntz D, Haas T (1996) Modelling of a trickle-bed reactor II. The hydrogenation of 3-hydroxypropanal to 1,3-propanediol. Chem Eng Process 35(1):11–19. https://doi.org/10.1016/0255-2701(95)04101-X